Inorganic Chemistry

Article

pubs.acs.org/IC

Polyoxometalate-Incorporated Metallapillararene/Metallacalixarene Metal-Organic Frameworks as Anode Materials for Lithium Ion Batteries

Xi-Ya Yang,[†,‡,⊥] Tao Wei,[§,∥,⊥] Ji-Sen Li,[‡] Ning Sheng,[‡] Pei-Pei Zhu,[†,‡] Jing-Quan Sha,*[,†,‡] Tong Wang,[‡] and Ya-Qian Lan*[,§]

[†]School of Pharmacy, Jiamusi University, HeilongJiang 154007, People's Republic of China

[‡]Key Laboratory of Inorganic Chemistry in Universities of Shandong, Department of Chemistry and Chemical Engineering, Jining University, Shandong 273155, People's Republic of China

[§]Jiangsu Key Laboratory of Biofunctional Materials, College of Chemistry and Materials Science, Nanjing Normal University, Nanjing 210023, People's Republic of China

[∥]School of Energy and Power, Jiangsu University of Science and Technology, Zhenjiang 212003, People's Republic of China

Supporting Information

ABSTRACT: A series of remarkable crystalline compounds containing metallapillararene/metallacalixarene metal-organic frameworks (MOFs), $[Ag_5(pyttz)_3{\cdot}Cl{\cdot}(H_2O)][H_3SiMo_{12}O_{40}]{\cdot}3H_2O$ (**1**), $[Ag_5(trz)_6][H_5SiMo_{12}O_{40}]$ (**2**), $[Ag_5(trz)_6][H_5GeMo_{12}O_{40}]$ (**3**), and $[Ag_5(trz)_6][H_4PW_{12}O_{40}]$ (**4**) (pyttz = 3-(pyrid-4-yl)-5-(1*H*-1,2,4-triazol-3-yl)-1,2,4-triazolyl, trz = 1,2,4-triazole), have been obtained by using a simple one-step hydrothermal reaction of silver nitrate, pyttz for **1** and trz for **2**–**4**, and Keggin type polyoxometalates (POMs). Crystal analysis reveals that Keggin POMs have been successfully incorporated in the windows of the metallapillararene/metallacalixarene MOFs in compounds **1**–**4**. In addition, the Keggin silicomolybdenate-based hybrid compounds **1** and **2** were used as anode materials in lithium ion batteries (LIBs), which exhibited promising electrochemical performance with the first discharge capacities of 1344 mAh g^{-1} for **1** and 1452 mAh g^{-1} for **2**, and this stabilized at 520 mAh g^{-1} for **1** and 570 mAh g^{-1} for **2** after 100 cycles at a current density of 100 mA g^{-1}. The performances are better than that of $(NBu_4)_4[SiMo_{12}O_{40}]$ matrix and commercial graphite anodes.

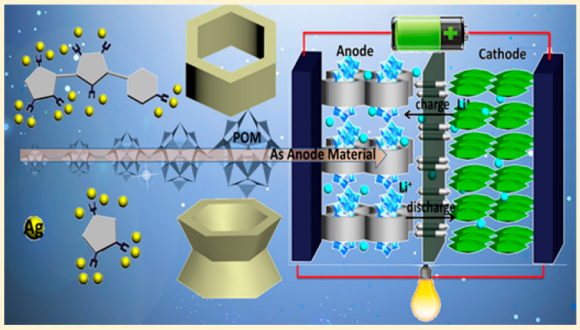

INTRODUCTION

Developing high-performance rechargeable batteries is one of the most important global issues to resolve the growing public concerns about environmental issues.[1−4] At present, lithium ion batteries (LIBs) have displayed huge prospects and have become promising energy storage systems for various electronic devices and vehicles due to their high energy densities.[5−8] However, graphite, as the most commonly used commercial LIB anode, possesses low theoretical capacity (<372 mAh g^{-1}) and limited capacity (<300 mAh g^{-1}) based on staging-type insertion reactions.[9−11] Thus, the development of new alternative anode materials for LIBs with high capacity and rate and stable cycle performance need to be explored. Recently, polyoxometalates (POMs), as one kind of significant metal oxide cluster with nanosizes and redox properties,[12−15] are expected to be candidates as anode materials for rechargeable LIBs owing to their reversible multielectron redox behavior[16,17] and electron storage functions.[18] However, the electronic conductivity of POMs from the molecular metal−oxo structure is low and POMs are prone to dissolve in electrolyte[19,20] due to their low specific surface area and poor stability,[21,22] which hinder their applications as anode materials for LIBs. Very recently, single-crystal materials with POMs incorporated into metal-organic frameworks (POMOFs) were applied in LIBs as the anode materials owing to their regular structure; they display a quite good reversible capacity of 540 mAh g^{-1} at a current rate of 0.25 C for $\{[Ni_6(OH)_3(H_2O)(en)_3(PW_9O_{34})][Ni_6(OH)_3(H_2O)_4(en)_3(PW_9O_{34})](BDC)_{1.5}\}[Ni(en)(H_2O)_4]$[23] and 587 mAh g^{-1} at a current rate of 0.1 C for $Na[Ag_{16}(Trz)_9(H_2O)_4][P_2W_{18}O_{62}]{\cdot}H_2O$[24] (Table S1 in the Supporting Information). However, due to the size of the gigantic POMOFs, they will have more space to incorporate POMs into diverse structural MOFs toward excellent electrochemistry performances.

It is known that a macrocyclic molecule, such as bowl-shaped calixarene or pillar-shaped pillararene, is one kind of excellent host matrix because of the flexible cavities.[25−27] In particular,

Received: April 19, 2017
Published: June 24, 2017

ACS Publications © 2017 American Chemical Society

DOI: 10.1021/acs.inorgchem.7b00995
Inorg. Chem. 2017, 56, 8311−8318

Table 1. Crystal Data for Compounds 1−4

	1	2	3	4
chem formula	$C_{27}H_{21}Ag_5ClMo_{12}N_{21}O_{44}Si$	$C_{12}H_5Ag_5Mo_{12}N_{18}O_{40}Si$	$C_{12}H_5Ag_5Mo_{12}N_{18}O_{40}Ge$	$C_{12}H_4Ag_5N_{18}O_{40}W_{12}P$
formula wt	3097.74	2759.96	2804.48	3816.78
temp (K)	298	293	293	293
wavelength (Å)	71.073	71.073	71.073	71.073
cryst syst	trigonal	trigonal	trigonal	trigonal
space group	$R\bar{3}$	$P\bar{3}_1m$	$P\bar{3}_1m$	$P\bar{3}_1m$
a (Å)	14.31	12.14	12.17	12.18
b (Å)	14.31	12.14	12.17	12.18
c (Å)	55.75	10.47	10.49	10.44
α (deg)	90	90	90	90
β (deg)	90	90	90	90
γ (deg)	120	120	120	120
V (Å^3)/Z	9885.8/6	1336.46/1	1345.70/1	1341.57/1
density (g cm^{-3})	3.119	3.423	3.454	4.719
abs coeff (mm^{-1})	5.677	6.426	6.902	29.308
F(000)	8694.0	1271.0	1289.0	1929
data collecn θ range (deg)	3.308−25.000	3.356−24.975	3.348−24.999	3.345−26.357
no. of rflns collected	6781	9241	2829	3180
no. of indep rflns	3872	860	867	1001
R_{int}	0.0228	0.0255	0.0283	0.0277
no. do data/restraints/params	3872/0/334	860/0/83	867/0/83	1001/6/83
final R indices ($I > 2\sigma(I)$)[a]	R1 = 0.041, wR2 = 0.089	R1 = 0.055, wR2 = 0.130	R1 = 0.059, wR2 = 0.139	R1 = 0.0820, wR2 = 0.1896
R indices (all data)[a]	R1 = 0.0539, wR2 = 0.0948	R1 = 0.0580, wR2 = 0.1326	R1 = 0.0703, wR2 = 0.1501	R1 = 0.0933, wR2 = 0.1990
largest diff peak and hole (e Å^{-3})	1.613 and −1.944	0.779 and −1.535	1.049 and −1.482	1.692 and −2.414

[a] $R1 = \sum(||F_o| - |F_c||)/\sum|F_o|$; $wR2 = \sum w(|F_o|^2 - |F_c|^2)^2/\sum w(|F_o|^2)^2]^{1/2}$.

the study of metallacalixarenes and metallapillararenes has attracted the interest of chemist because the inorganic units of the metallamacrocycle are metal ions and metal oxides, which can serve as redox-active sites during the electrochemical process.[28,29] In 1992, metallacalixarenes were initially defined as a class of metallacycle, in which the metal ions replace the CH_2 groups of classical calixarenes and the calixarene phenol rings are replaced by ditopic N-heterocyclic arene ligands, mimicking calixarene walls.[30] Until 2010, the first POM incorporating a metallacalixarene, $[Cu_{12}(C_7H_{12}N_8S_2)_9(HSiW_{12}O_{40})_4]$, was reported by Wang and co-workers.[31] In comparison with calixarene, pillararenes were first reported by Ogoshi in 2008.[32] In 2013, Dehaen's group introduced −S−CH_2− and −S−S− groups bridging between two benzene rings, obtaining new sulfur-bridged pillararene-like molecules.[33] In 2016, a new metal-organic host pillarplex (termed metallapillararenes) was reported by Pöthig using imidazolylidene and pyrazolato ligands to replace the hydroquinone units of classical pillararenes.[34] However, POM-incorporated metallapillararenes have not yet been explored thus far, to the best of our knowledge.

In this work, we report one POM-incorporated metallapillararene MOF, $[Ag_5(pyttz)_3{\cdot}Cl{\cdot}(H_2O)][H_3SiMo_{12}O_{40}]{\cdot}3H_2O$ (**1**), and three metallacalixarene MOFs, $[Ag_5(trz)_6][H_5SiMo_{12}O_{40}]$ (**2**), $[Ag_5(trz)_6][H_5GeMo_{12}O_{40}]$ (**3**), and $[Ag_5(trz)_6][H_4PW_{12}O_{40}]$ (**4**) (pyttz = 3-(pyrid-4-yl)-5-(1*H*-1,2,4-triazol-3-yl)-1,2,4-triazolyl, trz = 1,2,4- triazole). X-ray diffraction analysis clearly reveals the metallapillararene and metallacalixarene MOFs incorporating the POM nature. In particular, metallapillararene (**1**) and metallacalixarene (**2**) MOFs incorporating $[SiMo_{12}O_{40}]^{4-}$ polyoxoanions exhibit promising electrochemical performances when they are employed as the anode materials in lithium ion batteries (LIBs), which represents the first application-directed study for Keggin silicomolybdenate based hybrid compounds in LIBs.

EXPERIMENTAL SECTION

Materials and Methods. All reagents were commercially purchased and used as received, unless otherwise noted. All syntheses were carried out in 20 mL polytetrafluoroethylene lined stainless steel containers under autogenous pressure. Elemental analyses for C, H, and N were performed on a PerkinElmer 2400 CHN Elemental Analyzer. The IR spectra were obtained on an Alpha Centauri FT/IR spectrometer with KBr pellets in the 400−4000 cm^{-1} region. The XRPD patterns were obtained with a Rigaku D/max 2500 V PC diffractometer with Cu Kα radiation; the scanning rate was 4°/s, with 2θ ranging from 5 to 40°. The thermogravimetric analyses (TGA) were carried out on a PerkinElmer-7 thermal analyzer at a heating rate of 10 °C min^{-1}.

Synthesis of $[Ag_5(pyttz)_3{\cdot}(H_2O){\cdot}Cl][H_3SiMo_{12}O_{40}]{\cdot}3H_2O$ (1). $H_4SiMo_{12}O_{40}{\cdot}xH_2O$ and $H_4GeMo_{12}O_{40}{\cdot}xH_2O$ were synthesized according to the reported method.[35] $H_4SiMo_{12}O_{40}$ (300 mg, 0.16 mmol), $AgNO_3$ (150 mg, 0.89 mmol), and pyttz (70 mg, 0.33 mmol) were dissolved in distilled water (10 mL) with stirring for 0.5 h at room temperature, and the pH value was adjusted to ca. 1.5 by 1 mol L^{-1} HCl. The resulting solution was transferred into the 20 mL polytetrafluoroethylene-lined stainless steel reactor and heated at 160 °C for 3 days. After the autoclave was cooled to room temperature at 10 °C h^{-1}, yellow block crystals suitable for X-ray crystallography were obtained and then washed with distilled water and air-dried (yield 48% based on Ag). Anal. Calcd for $C_{27}H_{21}Ag_5ClMo_{12}N_{21}O_{44}Si$ (3097.74): C, 10.47; H, 0.68; N, 9.50. Found: C, 10.42; H, 0.84; N, 9.46. IR spectra (Figure S8 in the Supporting Information): characteristic bands at 952, 909, and 789 cm^{-1} are attributed to ν(Mo═O), ν(Si−O), and ν(Mo−O−Mo) vibrations, bands in the region of 1644−1109 cm^{-1} are attributed to the pyttz ligand.

Synthesis of $[Ag_5(trz)_6][H_5SiMo_{12}O_{40}]$ (2). $H_4SiMo_{12}O_{40}$ (300 mg, 0.16 mmol), $AgNO_3$ (150 mg, 0.89 mmol), and trz (50 mg, 0.72 mmol) were dissolved in distilled water (10 mL) with stirring for 0.5 h at room temperature, and the pH value was adjusted to ca. 2.0 by 1

DOI: 10.1021/acs.inorgchem.7b00995
Inorg. Chem. 2017, 56, 8311−8318

mol L^{-1} HCl. The resulting solution was transferred into the 20 mL polytetrafluoroethylene-lined stainless steel reactor and heated at 170 °C for 3 days. After the autoclave was cooled to room temperature at 10 °C h^{-1}, yellow block crystals suitable for X-ray crystallography were obtained and then washed with distilled water and air-dried (yield 48% based on Ag). Anal. Calcd for $C_{12}H_5Ag_5Mo_{12}N_{18}O_{40}Si$, (2759.96): C, 5.22, H, 0.18, N, 9.14. Found C, 5.19; H, 0.25; N, 9.11. IR spectra (Figure S8 in the Supporting Information): characteristic bands at 962, 906, and 787 cm^{-1} are attributed to ν(Mo═O), ν(Si−O), and ν(Mo−O−Mo) vibrations, bands in the region of 1632−1148 cm^{-1} are attributed to the pyttz ligand.

Synthesis of $[Ag_5(trz)_6][H_5GeMo_{12}O_{40}]$ (3). $H_4GeMo_{12}O_{40}{\cdot}xH_2O$ was synthesized according to the reported method.[35] Compound **3** was prepared in a manner similar to that described for **2**, except that $H_4GeMo_{12}O_{40}$ (300 mg, 0.16 mmol) replaced $H_4SiMo_{12}O_{40}$. Yellow block crystals were obtained (yield 36% based on Ag). Anal. Calcd for $C_{12}H_5Ag_5Mo_{12}N_{18}O_{40}Ge$, (2804.48): C, 5.14; H, 0.18; N, 8.99. Found: C, 5.13; H, 0.22; N, 8.96. IR spectra (Figure S8 in the Supporting Information): characteristic bands at 950, 887, and 775 cm^{-1} are attributed to ν(Mo═O), ν(Ge−O), and ν(Mo−O−Mo) vibrations, bands in the region of 1637−1154 cm^{-1} are attributed to the pyttz ligand.

Synthesis of $[Ag_5(trz)_6][H_4PW_{12}O_{40}]$ (4). Compound **4** was prepared in a manner similar to that described for **2**, except that $H_3PW_{12}O_{40}$ (300 mg, 0.10 mmol) replaced $H_4SiMo_{12}O_{40}$. Yellow block crystals were obtained (yield 58% based on Ag). Anal. Calcd for $C_{12}H_4Ag_5N_{18}O_{40}W_{12}P$, (3816.78): C, 3.78; H, 0.11; N, 6.61. Found: C, 3.75; H, 0.20; N, 6.56. IR spectra (Figure S8 in the Supporting Information): characteristic bands at 1075, 959, and 793 cm^{-1} are attributed to ν(P−O), ν(W═O), and ν(W−O−W) vibrations, bands in the region of 1644−1109 cm^{-1} are attributed to the pyttz ligand.

Battery Analyses. The as-prepared compounds **1** and **2** and $(NBu_4)_4[SiMo_{12}O_{40}]$ were used as the anode materials to study their respective electrochemical performances in LIBs. By mixing each compound, Super-P carbon, and polyvinylidene fluoride (PVDF) at a weight ratio of 7:2:1, we obtained the anodes. Then we added *N*-methyl-2-pyrrolidinone (NMP) to the mixture to form a paste with appropriate viscosity. The paste was mildly coated on pure Cu foil and vacuum-dried at 50 °C for 24 h. The loading mass of electroactive materials in the electrode slurry is ∼2 mg cm^{-2}. The testing coin cells were assembled in an argon-filled glovebox with the working electrode as fabricated, metallic lithium foil as the counter electrode, and 1.0 M $LiPF_6$ in ethylene carbonate/diethyl carbonate (1/1 v/v) as the electrolyte. Galvanostatic charge/discharge cycles were performed on a LAND 2001A instrument (Wuhan, China) and electrochemical workstation (Princeton Applied Research, Germany) to record the circulation measurements, and cyclic voltammetry (CV) and electrochemical impedance spectroscopy (EIS) of batteries was carried out at constant ambient temperature. The specific capacity was calculated on the basis of the mass of active material.

X-ray Crystallographic Study. Crystallographic data for compounds **1**−**4** were collected on an Agilent Technology Eos Dual system with Mo Kα radiation (λ = 0.71069 Å) at 293 K. The structures were solved by direct methods and refined with full-matrix least squares on F^2 through the SHELXTL and WINGX software package.[36] All non-hydrogen atoms were refined anisotropically, and the "ISOR" command was used to refine some APD problems. Crystal data and structure refinement details for compounds **1**−**4** are given in Table 1. The crystallographic data have been deposited with the Cambridge Crystallographic Data Centre (CCDC) as entries 1513351 (**1**), 1513352 (**2**), 1513354 (**3**), and 1513353 (**4**). Selected bond lengths and angles of **1**−**4** are given in Tables S3−S6 in the Supporting Information.

RESULTS AND DISCUSSION

Single-crystal X-ray diffraction analysis reveals that **1** is constructed by 2D $[Ag_5(pyttz)_3{\cdot}(H_2O){\cdot}Cl]_n$ MOFs with a metallapillar[6]arene host matrix and Keggin POMs as guest molecules. Compounds **2**−**4** are isostructural and exhibit the 3D framework constructed by 2D $[Ag_5(trz)_6]_n$ MOFs with a metallacalix[6]arene host matrix and covalently linking Keggin POMs as guest molecules. The valence sum calculations[37] show that all W/Mo atoms are in the +VI oxidation state and all Ag ions are in the + oxidation state, which was confirmed by crystal color, charge neutrality, and coordination environments. To balance the charge, some protons are added into POMs, and then **1** is formulated as $[Ag_5(pyttz)_3{\cdot}(H_2O){\cdot}Cl][H_5SiMo_{12}O_{40}]{\cdot}3H_2O$, **2** and **3** are formulated as $[Ag_5(trz)_6][H_5XMo_{12}O_{40}]$ (X = Si for **2**, X = Ge for **3**), and **4** is formulated as $[Ag_5(trz)_6][H_4PW_{12}O_{40}]$.

Structural Description of Compound 1. Compound **1** consists of five Ag^+ ions, three pyttz ligands, one chloride ion, and one $[SiMo_{12}O_{40}]^{4-}$ polyoxoanion (abbreviated as $SiMo_{12}$), as shown in Figure S1 in the Supporting Information, and crystallizes in the space group $R\bar{3}$ with six formula units in the unit cell. There are three crystallographically independent Ag ions (Ag1, Ag2, and Ag3) and one deprotonated pyttz ligand, and their coordination modes are illustrated in Figure S1. The bond lengths around Ag ions are in the range of 3.121−3.139 Å for Ag−Ag bonds, 2.587−2.767 Å for Ag−Cl bonds, and 2.260−2.311 Å for Ag−N bonds, while the N−Ag−N angles are in the range of 72.7−142.6°.

Without regard to the $SiMo_{12}$ polyoxoanion, the most interesting structural feature is that the 30-nuclear silver metallapillararene containing two kinds of loops is successfully fabricated by 6 Ag1, 6 Ag2, and 18 Ag3 ions with chloride ions and pyttz ligands. More specifically, 6 Ag3 ions with 6 pyttz ligands form a hexanuclear $[Ag_6(pyttz)_6]$ loop called the inner loop with dimensions of approximately 11.930 Å × 11.930 Å (loop A, Figure 1a). In addition, 12 Ag3 ions with 6 pyttz ligands and 6 chloride ions form a 12-nuclear $[Ag_{12}Cl_6(pyttz)_6]$

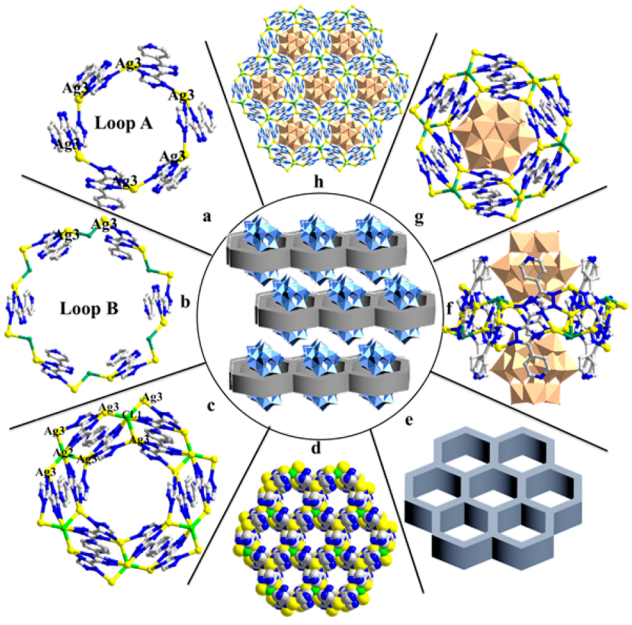

Figure 1. Ball and stick representation of the inner loop (a), the outer loop (b), and the 30-nuclear silver metallapillararene subunit (c) of **1**. Space-filling (d) and schematic representations (e) of 2D pillararene-like MOFs (each metallapillararene can be simplified as a hexagon) of **1**. Combined polyhedron and ball and stick representation of the $SiMo_{12}$ polyoxoanion located at the windows of the pillararene in different orientations in **1** (f, g). Representation of the 2D (h) and 3D (middle) POM incorporated metallapillararene MOFs in **1**.

DOI: 10.1021/acs.inorgchem.7b00995
Inorg. Chem. 2017, 56, 8311−8318

loop called the outer loop with dimensions of approximately 16.625 Å × 16.625 Å (loop B, Figure 1b). Driven by the pyttz molecules containing a longer and rigid spacer, the inner loop A and outer loop B connect each other, giving a double-layer $[Ag_{30}Cl_6(pyttz)_{12}]$ metallapillar[6]arene via the Ag−N (Ag1−N3 and Ag2−N4) and Ag−Cl (Ag1−Cl and Ag3−Cl) bonds (Figure 1c and Figure S2 in the Supporting Information), in which Ag1 and Ag2 ions as their common vertexes stabilize the metallapillararene subunit. Note that the argentophilic Ag^+−Ag^+ interactions[38,39] ($D_{Ag1-Ag2}$ = 3.121 Å and $D_{Ag1-Ag3}$ = 3.139) also contribute greatly to the formation of the metallapillarene unit (Figure S2). Then each metallapillararene links with 6 of the surrounding same subunits, generating an extended 2D pillararene-like MOF by sharing the sides of the inner and outer loops (Figure 1d,e and Figure S3 in the Supporting Information). Moreover, the $SiMo_{12}$ polyoxoanions as non-coordinated guest molecules are located at the windows of the pillararene via weak interactions ($O_7\cdots N_7$ = 2.88 Å, $O_{13}\cdots N_1$ = 2.92 Å), forming 2D POMs incorporating metallapillararene MOFs with POM−$[Ag_{30}Cl_6(pyttz)_{12}]$−POM sandwich structures (Figure 1f−h). Finally, the adjacent metallapillararene layers extend into a 3D supramolecule in a staggered mode via O···O interactions (Figure 1, middle, and Figure S4 in the Supporting Information).

Structural Description of Compounds 2−4. Single-crystal X-ray diffraction analysis reveals that compounds **2**−**4** are isostructural and consist of five Ag^+ ions, six deprotonated trz ligands, and one Keggin polyoxoanion ($[SiMo_{12}O_{40}]^{4-}$, abbreviated as $SiMo_{12}$ for **2**; $[GeMo_{12}O_{40}]^{4-}$, abbreviated as $GeMo_{12}$ for **3**; $[PW_{12}O_{40}]^{3-}$ abbreviated as PW_{12} for **4**), as shown in Figure S1 in the Supporting Information, and crystallize in the space group $P\bar{3}_1m$ with one formula unit in the unit cell. In **2**, there is one crystallographically independent $SiMo_{12}$ polyoxoanion, one disordered trz ligand, and two crystallographically unique Ag ions (Ag1 and Ag2), and their coordination modes are illustrated in Figure S1. The bond lengths around Ag ions are in the range of 2.931 Å for Ag−O bonds and 2.260−2.761 Å for Ag−N bonds, while the N−Ag−N angles are in the range of 117.5−166.5°.

Without regard to the $SiMo_{12}$ polyoxoanion, six Ag1 ions with six trz ligands also fabricate a hexanuclear $[Ag_6(trz)_6]$ metallacycle (Figure 2a), in which each trz ligand adopts a pyrazole-like configuration. Different from compound **1**, two $[Ag_6(trz)_6]$ subunits connect with six Ag2 ions, forming a $\{Ag_6[Ag_6(trz)_6]_2\}$ double metallacalix[6]arene with dimensions of approximately 9.4 Å × 9.4 Å (Figure 2b), in which six Ag2 ions construct a hexagon symmetrical plane (Figure 2c). Then, like **1**, each metallacalixarene links with the surrounding six same subunits, generating extended 2D calixarene-like MOFs by sharing sides (Figure 2d,e and Figure S5 in the Supporting Information), which is also a new member of the metallacalixarene family. In turn, without regard to the organic ligands, each $SiMo_{12}$ polyoxoanion connects with 12 Ag2 ions (Figure 2f), forming a POM−Ag chain as shown in Figure S6 in the Supporting Information. As a result, the POM−Ag 1D chains and 2D $[Ag_2(trz)_3]_n$ MOFs connect together, fabricating a 3D framework (Figure 2h and middle), in which the $SiMo_{12}$ clusters are located in the center of channels formed by the adjacent 2D $[Ag_2(trz)_3]_n$ MOFs via Ag−O bonds (Figure 2g and Figure S7 in the Supporting Information). This is also true for **3** and **4**.

Compounds **1**−**4** were synthesized under the same reaction conditions except for the different natural ligands: pyttz for **1** and trz for **2**−**4**. As a result, two distinct metallamacrocycles, the 30-nuclear metallapillararenes for **1** and the 18-nuclear metallacalixarenes for **2**−**4**, were obtained. Unambiguously, the organic ligands dominate the structural formation of the resultant compounds, which can be summarized in Figure 3. More specifically, six Ag ions in the inner loop of metallapillararenes for **1** are deactivated due to the chelated coordination of pyttz and argentophilic Ag−Ag interactions,

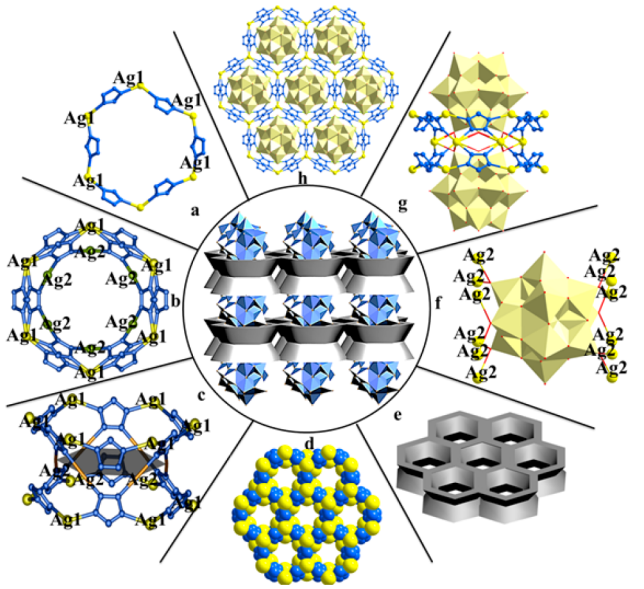

Figure 2. Ball and stick representation of the hexanuclear $[Ag_6(trz)_6]$ unit (a) and the 18-nuclear silver metallacalixarenes (b) for **2**−**4**. Representation of the hexagon symmetrical plane of metallacalixarenes constructed by six Ag2 ions (c) for **2**−**4**. Space-filling (d) and schematic representations (e) of 2D calixarene-like MOFs (each metallacalixarene can be simplified as a cuplike hexagon) for **2**−**4**. Combined polyhedron and ball and stick representation of $SiMo_{12}$ polyoxoanion as a 12-linker (f) located at the windows of the metallacalixarenes (g) for **2**−**4**. Representation of the 2D (h) and 3D (middle) POM incorporated metallacalixarene MOFs for **2**−**4**.

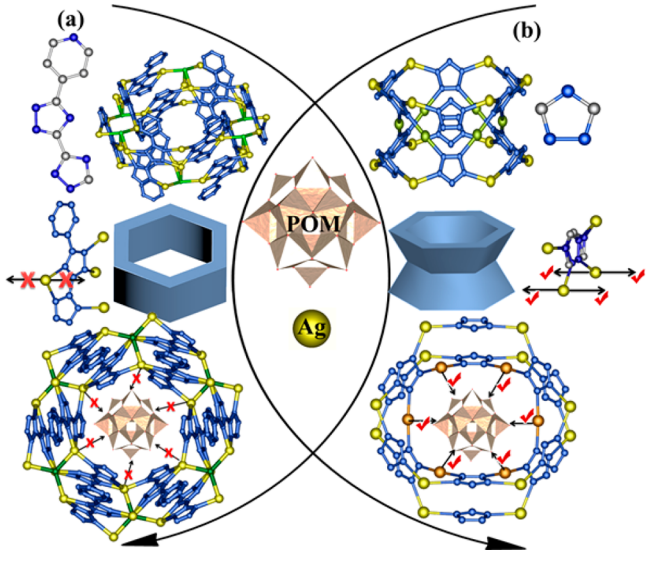

Figure 3. Representation of the influence of the pyttz and trz ligands on the construction of metal organic macrocycle building block in compounds **1** and **2**−**4**.

DOI: 10.1021/acs.inorgchem.7b00995
Inorg. Chem. 2017, 56, 8311−8318

which make it difficult to support a further extension. All these factors mean that Ag3 ions cannot coordinate with oxygen atoms of $SiMo_{12}$ polyoxoanion, which results in the formation of metallapillararenes and $SiMo_{12}$ polyoxoanions only as noncoordinated guest molecules located at the windows of the metallapillararenes. In comparison with **1**, Ag ions with trz molecules possess more flexible extended modes in compounds **2**−**4**, which increases the coordinating opportunities with POMs and Ag ions, so that each $SiMo_{12}$ polyoxoanion can bind six Ag2 ions from the same symmetrical plane, shrinking the dimensions of the central metallacycleand resulting in the formation of metallacalixarenes.

XRD Pattern and TG Analyses. The XRPD patterns for compounds **1**−**4** are presented in the Figure S9 in the Supporting Information. The diffraction peaks of both simulated and experimental patterns match well, thus indicating that the phase purity of the compounds is good. The thermal stability curves are shown in Figure S10 in the Supporting Information. For compound **1**, the thermal analysis exhibit two steps of weight loss: the first loss is 2.43% at 40−200 °C corresponding to the loss of all water (calculated 2.32%), and the second loss is 20.54% (calculated 20.56%) at 350−530 °C arising from the decomposition of the pyttz organic molecules. For compounds **2** and **3**, the thermal analysis shows similar steps of weight loss; more specifically, the total weight loss is 14.87% (calculated 14.80%) for **2**, 14.62% (calculated 14.56%) for **3**, and 10.56% (calculated 10.70%) for **4**, which corresponds to the decomposition of the trz organic molecules. The weight loss agrees with the calculated values for compounds **1**−**4**.

Electrochemical Performance. Toward exploring the potential application of these newly prepared POM-incorporated metallapillararene/metallacalixarene MOFs, initial studies on the electrochemical properties of the **1** and **2** as anode materials for LIBs were carried out. Figure 4 shows the cyclic

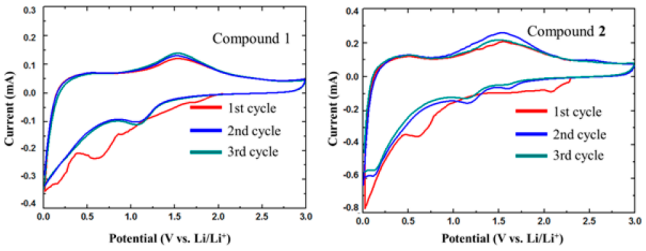

Figure 4. Cyclic voltammograms for compounds **1** (left) and **2** (right) as anode materials in the range of 0−3 V (scan rate 0.1 mV s^{-1}).

voltammograms (CVs) of **1** and **2** in the range of 0.01−3 V (scan rate 0.1 mV s^{-1}). The irreversible reduction peaks around 0.65 V at the first cycle that disappear in the subsequent cycles should be due to the formation of solid electrolyte interphase (SEI) films in both **1** and **2** (as seen in Figure S11 in the Supporting Information, with compound **2** as an example), which frequently occurs in LIBs.[40,41] The reduction peak observed at 0.01−0.2 V is due to the insertion of Li^+ into the anode materials.[24] In the subsequent cycles (for both compounds), two distinct peaks become visible at a potential of about 1.25 V for the reduction and 1.50 V for the oxidation, indicating a defined electrochemical process, which may be ascribed to the reduction and oxidation of the Mo^{6+}.[41]

To understand the influence of POM-incorporated metallapillararene/metallacalixarene MOFs on the battery performance, the insoluble $(NBu_4)_4[SiMo_{12}O_{40}]$ matrix was chosen. As shown in Figure 5, the initial discharge capacities of **1** and **2** are 1344 and 1452 mAh g^{-1}, respectively, while the first discharge

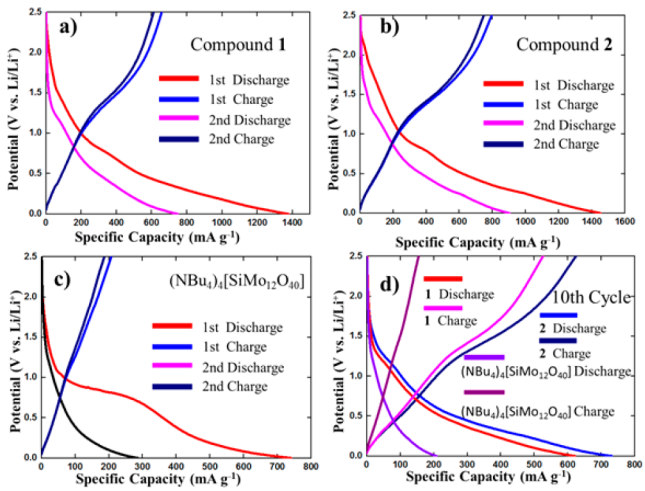

Figure 5. Galvanostatic charge−discharge curves of (a) **1**, (b) **2**, and (c) $(NBu_4)_4[SiMo_{12}O_{40}]$ anodes during the initial two cycles and galvanostatic charge−discharge curves at the 10th cycle at a current density of 100 mA g^{-1} (d).

capacity of $(NBu_4)_4[SiMo_{12}O_{40}]$ is only 740 mAh g^{-1} at a current density of 100 mA g^{-1}, all of which are still much better than that for commercial graphite.[24] At the second cycle, the discharge capacity decreased to 752 mAh g^{-1} for **1** and 901 mAh g^{-1} for **2**, probably due to the formation of the solid electrolyte interphase (SEI) films, while that for $(NBu_4)_4[SiMo_{12}O_{40}]$ decreased to 286 mAh g^{-1}. Obviously, the capacities of **1** and **2** anodes are significantly higher than that of $(NBu_4)_4[SiMo_{12}O_{40}]$, which may be the contribution of the synergistic effect between POMs and the metallapillararene/metallacalixarene matrix. In addition, in order to further explore the battery performances, the cycling stabilities of **1** and **2** as anode materials were also studied. As shown in Figure 6,

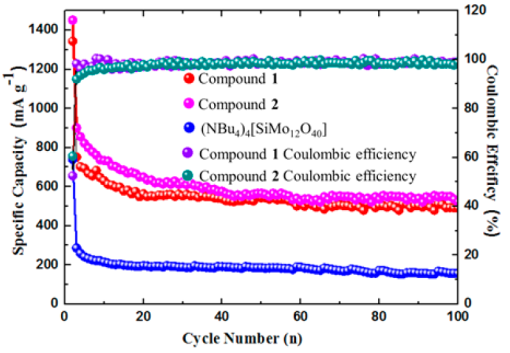

Figure 6. Discharge capacity and Coulombic efficiency of these anodes at a current density of 100 mA g^{-1}.

after 35 cycles, the cycling capacity maintains stable at ca. 520 mAh g^{-1} for **1** and 570 mAh g^{-1} for **2** after 100 cycles at a current density of 100 mA g^{-1}. It is worth noting that the Coulombic efficiencies of **1** and **2** can all reach above 99% after 40 cycles, where they remain stable, which indicates their commendable cycling stabilities. In comparison, the capacity of $(NBu_4)_4[SiMo_{12}O_{40}]$ changes to ca. 170 mAh g^{-1} after 100 cycles at the same current density. As a result, the superior

DOI: 10.1021/acs.inorgchem.7b00995
Inorg. Chem. 2017, 56, 8311−8318

capacity and stability of anodes **1** and **2** over $(NBu_4)_4[SiMo_{12}O_{40}]$ can be believed to be closely associated with the metallapillararene/metallacalixarene host matrix, which possesses a stabilized crystal structure and provides a stable charge transfer route.

Usually, the rate performance of LIBs is the decisive factor for practical applications. As shown in Figure 7, **1** and **2** anodes

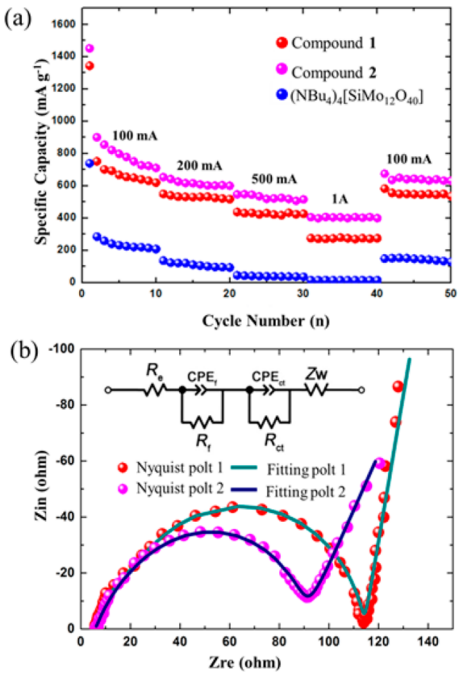

Figure 7. (a) Rate performance of **1**, **2**, and $(NBu_4)_4[SiMo_{12}O_{40}]$ anodes at current densities of 100 mA g^{-1} to 1 A g^{-1}. (b) Nyquist plots and fitting plots of **1** and **2** anodes after the first discharge−charge process. Insert: the simulated equivalent circuit of the electrode/electrolyte interface.

show good rate performances at current densities from 100 mA g^{-1} to 1 A g^{-1}. The reversible capacities of **1** and **2** at 100 mA g^{-1} are 550 and 640 mAh g^{-1} after an initial drop, respectively; when the current density was 1 A g^{-1}, the capacities of **1** and **2** were maintained at 270 and 370 mAh g^{-1}, respectively. When the current density was set back to 100 mA g^{-1} after 40 cycles, the capacities were almost restored to the original specific capacities. In contrast, the capacity of the $(NBu_4)_4[SiMo_{12}O_{40}]$ anode is much lower than that of other anodes at each current density. In our previous work, we used commercial graphite as anodes for LIBs and studied its cycling and rate performance. The reversible capacities of graphite at 100 mA g^{-1} are 320 mA h g^{-1} after initial drop and are retained at 200 mA h g^{-1} at 1 A g^{-1}. Therefore, compound **1** and **2** have a greater advantage than graphite.

Electrochemical impedance spectroscopy (EIS) was used to evaluate the electrochemical behavior of **1** and **2** anodes, and the equivalent circuit model was introduced into the analysis system (Figure 7b). In the circuit model R_e, R_f and R_{ct} represent the electrolyte resistance, SEI film resistance, and the charge-transfer resistance, respectively. The Warburg impedance (Zw) represents the diffusion of Li^+ ions into the bulk electrode. CPE_f and CPE_{ct} both represent the constant-phase element. The values of R_f and R_{ct} are 21.0 and 88.2 Ω for **1** and 27.5 and 53.8 Ω for **2**, respectively. The sums of resistances are 114.6 for **1** and 87.1 for **2**, which are much smaller than those of POM-based coordination polymers (POMCPs) in our previous work.[24] This indicates that the Keggin silicomolybdenate incorporated metallapillararene/metallacalixarene compounds can support a pathway for fast Li^+ ion transportation. In addition to that, compounds **1** and **2** as anode materials maintain good electron conductivities to improve the electrochemical performance in LIBs.

CONCLUSION

Briefly summarizing the results above, by employing conjugated heterocyclic pyttz and trz ligands, a series of Keggin POM incorporated metallapillararene/metallacalixarene MOFs were successfully isolated through self-organization, in which the coordination mode of the organic ligands dominates the structural formation of the resultant compounds; compound **1** represents the first example of metallapillararene-containing POMs to date. The application of **1** and **2** as anode materials in LIBs exhibits initial specific capacities of 1344 mAh g^{-1} for **1** and 1452 mAh g^{-1} for **2**, and the discharge capacity is stabilized at 570 mAh g^{-1} for **1** and 520 mAh g^{-1} for **2** after 100 cycles at a current density of 0.1 mA g^{-1}. These performances are much higher than those of $(NBu_4)_4[SiMo_{12}O_{40}]$ and commercial graphite. The present result indicates that POM-incorporated metallapillararene/metallacalixarene MOFs can provide a stable charge transmission route during the discharge−charge process. This is also the first time that POM-incorporated metallmacrocycle MOFs as anode materials for LIBs were studied. More efforts toward the design and synthesis of novel POMCPs with interesting structures and superior electrochemical performance need to be made.

ASSOCIATED CONTENT

Supporting Information

The Supporting Information is available free of charge on the ACS Publications website at DOI: 10.1021/acs.inorgchem.7b00995.

Selected bond lengths and bond angles for compounds **1**−**4** and IR, PXRD, TGA, and partial structural figures of compounds **1**-**4** (PDF)

Accession Codes

CCDC 1513351−1513354 contain the supplementary crystallographic data for this paper. These data can be obtained free of charge via www.ccdc.cam.ac.uk/data_request/cif, or by emailing data_request@ccdc.cam.ac.uk, or by contacting The Cambridge Crystallographic Data Centre, 12 Union Road, Cambridge CB2 1EZ, UK; fax: +44 1223 336033.

AUTHOR INFORMATION

Corresponding Authors

*E-mail for J.-Q.S.: shajq2002@126.com.
*E-mail for Y.-Q.L.: yqlan@njnu.edu.cn.

ORCID

Ya-Qian Lan: 0000-0002-2140-7980

Author Contributions

⊥X.-Y.Y. and T.W. contributed equally.

Notes

The authors declare no competing financial interest.

ACKNOWLEDGMENTS

This work was financially supported by the Talent Culturing Plan for Leading Disciplines of University in Shandong

DOI: 10.1021/acs.inorgchem.7b00995
Inorg. Chem. 2017, 56, 8311−8318

Province, NNSF (no. 21271089), the China Postdoctoral Science Foundation (2016M600914), the New Century Excellent Talents Program in Heilongjiang Province (1253-NCET-022), S&T innovation projects of graduate student in Jiamusi University (YM2016_106), and Jiangsu Planned Projects for Postdoctoral Research Funds (1601087C).

REFERENCES

(1) Tarascon, J. M.; Armand, M. Issues and challenges facing rechargeable lithium batteries. *Nature* **2001**, *414*, 359−367.
(2) Armand, M.; Tarascon, J. M. Building better batteries. *Nature* **2008**, *451*, 652−657.
(3) Fan, Q.; Liu, W.; Weng, Z.; Sun, Y.; Wang, H. Ternary hybrid material for high-performance lithium-sulfur battery. *J. Am. Chem. Soc.* **2015**, *137*, 12946−12953.
(4) Wang, C.; Jiang, C.; Xu, Y.; Liang, L.; Zhou, M.; Jiang, J. A Selectively Permeable Membrane for Enhancing Cyclability of Organic Sodium-Ion Batteries. *Adv. Mater.* **2016**, *28*, 9182−9187.
(5) Wang, H.; Hamanaka, S.; Nishimoto, Y.; Irle, S.; Yokoyama, T.; Yoshikawa, H.; Awaga, K. In operando X-ray absorption fine structure studies of polyoxometalate molecular cluster batteries: polyoxometalates as electron sponges. *J. Am. Chem. Soc.* **2012**, *134*, 4918−4924.
(6) Yim, T.; Han, S. H.; Park, N. H.; Park, M.; Lee, J. H.; Shin, J. Effective Polysulfide Rejection by Dipole-Aligned $BaTiO_3$ Coated Separator in Lithium−Sulfur Batteries. *Adv. Funct. Mater.* **2016**, *26*, 7817−7823.
(7) Xu, Y.; Zhu, Y.; Liu, Y.; Wang, C. Electrochemical performance of porous carbon/tin composite anodes for sodium-ion and lithium-ion batteries. *Adv. Energy Mater.* **2013**, *3*, 128−133.
(8) Yang, Z.; Xia, J.; Zhi, L.; Zhang, W.; Pei, B. An improved solid-state reaction route to Mg^{2+}-doped $LiFePO_4$/C cathode material for Li-ion battery. *Ionics* **2014**, *20*, 169−174.
(9) Aurbach, D.; Markovsky, B.; Weissman, I.; Levi, E.; Ein-Eli, Y. On the correlation between surface chemistry and performance of graphite negative electrodes for Li ion batteries. *Electrochim. Acta* **1999**, *45*, 67−86.
(10) Jang, B.; Park, M.; Chae, O. B.; Park, S.; Kim, Y.; Oh, S. M.; Piao, Y.; Hyeon, T. Direct synthesis of self-assembled ferrite/carbon hybrid nanosheets for high performance lithium-ion battery anodes. *J. Am. Chem. Soc.* **2012**, *134*, 15010−15015.
(11) Xue, D. J.; Xin, S.; Yan, Y.; Jiang, K. C.; Yin, Y. X.; Guo, Y. G.; Wan, L. J. Improving the electrode performance of Ge through Ge@ C core−shell nanoparticles and graphene networks. *J. Am. Chem. Soc.* **2012**, *134*, 2512−2515.
(12) Long, D. L.; Tsunashima, R.; Cronin, L. Polyoxometalates: building blocks for functional nanoscale systems. *Angew. Chem., Int. Ed.* **2010**, *49*, 1736−1758.
(13) von Allmen, K. D.; Grundmann, H.; Linden, A.; Patzke, G. R. Synthesis and Characterization of 0D − 3D Copper-Containing Tungstobismuthates Obtained from the Lacunary Precursor $Na_9[B\text{-}\alpha\text{-}BiW_9O_{33}]$. *Inorg. Chem.* **2017**, *56*, 327−335.
(14) Han, X. B.; Li, Y. G.; Zhang, Z. M.; Tan, H. Q.; Lu, Y.; Wang, E. B. Polyoxometalate-Based Nickel Clusters as Visible Light-Driven Water Oxidation Catalysts. *J. Am. Chem. Soc.* **2015**, *137*, 5486−5493.
(15) Wang, L. S.; Lu, Y.; Máille, G. M. Ó.; Anthony, S. P.; Nolan, D.; Draper, S. M. Sonogashira cross-coupling as a route to tunable hybrid organic−inorganic rods with a polyoxometalate backbone. *Inorg. Chem.* **2016**, *55*, 9497−9500.
(16) Coronado, E.; Gómez-García, C. J. Polyoxometalate-based molecular materials. *Chem. Rev.* **1998**, *98*, 273−296.
(17) Nyman, M.; Burns, P. C. A comprehensive comparison of transition-metal and actinyl polyoxometalates. *Chem. Soc. Rev.* **2012**, *41*, 7354−7367.
(18) Zhang, Z.; Yoshikawa, H.; Zhang, Z.; Murayama, T.; Sadakane, M.; Inoue, Y.; Hara, M. Synthesis of Vanadium-Incorporated, Polyoxometalate-Based Open Frameworks and Their Applications for Cathode-Active Materials. *Eur. J. Inorg. Chem.* **2016**, *2016*, 1242−1250.
(19) Ji, Y.; Huang, L.; Hu, J.; Chen, W.; Streb, C.; Song, Y. F. Polyoxometalate-functionalized nanocarbon materials for energy conversion, energy storage and sensor systems. *Energy Environ. Sci.* **2015**, *8*, 776−789.
(20) Xie, J. J.; Zhang, Y.; Han, Y. L.; Li, C. L. High-Capacity Molecular Scale Conversion Anode Enabled by Hybridizing Cluster-Type Framework of High Loading with Amino-Functionalized Graphene. *ACS Nano* **2016**, *10*, 5304−5313.
(21) Yu, R.; Kuang, X. F.; Wu, X. Y.; Lu, C. Z.; Donahue, J. P. Stabilization and immobilization of polyoxometalates in porous coordination polymers through host−guest interactions. *Coord. Chem. Rev.* **2009**, *253*, 2872−2890.
(22) Kozhevnikov, I. V. Catalysis by heteropoly acids and multicomponent polyoxometalates in liquid-phase reactions. *Chem. Rev.* **1998**, *98*, 171−198.
(23) Yue, Y.; Li, Y.; Bi, Z.; Veith, G. M.; Bridges, C. A.; Guo, B.; Chen, J.; Mullins, D. R.; Surwade, S. P.; Mahurin, S. M.; Liu, H.; Parans Paranthaman, M.; Dai, S. A POM−organic framework anode for Li-ion battery. *J. Mater. Chem. A* **2015**, *3*, 22989−22995.
(24) Li, M. T.; Cong, L.; Zhao, J.; Zheng, T. T.; Tian, R.; Sha, J. Q.; Su, Z. M.; Wang, X. L. Self-Organization towards Complex Multi-Fold Meso-Helixes in the Structures of Wells-Dawson Polyoxometalate Based Hybrid Materials for Lithium-Ion Batteries. *J. Mater. Chem. A* **2017**, *5*, 3371−3376.
(25) Böhmer, V. Calixarenes, macrocycles with (almost) unlimited possibilities. *Angew. Chem., Int. Ed. Engl.* **1995**, *34*, 713−745.
(26) Navarro, J. A.; Janik, M. B.; Freisinger, E.; Lippert, B. $[(Ethylenediamine)\ Pt\ (uracilate)]_4$, a Metal Analogue of Calix [4] arene. Coordination and Anion Host− Guest Chemistry Related to Its Conformational Dynamics. *Inorg. Chem.* **1999**, *38*, 426−432.
(27) Strutt, N. L.; Fairen-Jimenez, D.; Iehl, J.; Lalonde, M. B.; Snurr, R. Q.; Farha, O. K.; Hupp, J. T.; Stoddart, J. F. Incorporation of an A1/A2-difunctionalized pillar [5] arene into a metal−organic framework. *J. Am. Chem. Soc.* **2012**, *134*, 17436−17439.
(28) Chen, S.; Chen, L. J.; Yang, H. B.; Tian, H.; Zhu, W. Light-triggered reversible supramolecular transformations of multi-bisthienylethene hexagons. *J. Am. Chem. Soc.* **2012**, *134*, 13596.
(29) Xu, L.; Chen, L. J.; Yang, H. B. Recent progress in the construction of cavity-cored supramolecular metallodendrimers via coordination-driven self-assembly. *Chem. Commun.* **2014**, *50*, 5156−5170.
(30) Rauter, H.; Hillgeris, E. C.; Lippert, B. A cyclic tetranuclear platinum complex of uracil. *J. Chem. Soc., Chem. Commun.* **1992**, *19*, 1385−1386.
(31) Wang, X. L.; Hu, H. L.; Liu, G. C.; Lin, H. Y.; Tian, A. X. Self-assembly of nanometre-scale metallacalix [4] arene building blocks and Keggin units to a novel (3, 4)-connected 3D self-penetrating framework. *Chem. Commun.* **2010**, *46*, 6485−6487.
(32) Ogoshi, T.; Kanai, S.; Fujinami, S.; Yamagishi, T. A.; Nakamoto, Y. para-Bridged symmetrical pillar [5] arenes: their Lewis acid catalyzed synthesis and host−guest property. *J. Am. Chem. Soc.* **2008**, *130*, 5022−5023.
(33) Sonawane, M. P.; Jacobs, J.; Thomas, J.; Meervelt, L. V.; Dehaen, W. Synthesis and structural exploration of disulfide bridged [2n] pillararene-like molecules. *Chem. Commun.* **2013**, *49*, 6310−6312.
(34) Altmann, P. J.; Pöthig, A. Pillarplexes: A Metal−Organic Class of Supramolecular Hosts. *J. Am. Chem. Soc.* **2016**, *138*, 13171−13174.
(35) Rocchiccioli-Deltcheff, C.; Fournier, M.; Franck, R.; Thouvenot, R. Vibrational investigations of polyoxometalates. 2. Evidence for anion-anion interactions in molybdenum(VI) and tungsten(VI) compounds related to the Keggin structure. *Inorg. Chem.* **1983**, *22*, 207−216.
(36) Sheldrick, G. M. *SHELX-97, Program for Crystal Structure Refinement*; University of Göttingen, Göttingen, Germany, 1997.
(37) Brown, I. D.; Altermatt, D. Bond-valence parameters obtained from a systematic analysis of the Inorganic Crystal Structure Database. *Acta Crystallogr., Sect. B: Struct. Sci.* **1985**, *41*, 244−247.
(38) Gruber, F.; Jansen, M. Supramolecular Intercluster Compounds Consisting of 1D Arrays of Silver Alkynyl Clusters and Wells-Dawson

DOI: 10.1021/acs.inorgchem.7b00995
Inorg. Chem. 2017, 56, 8311−8318

Anions, Displaying Ligand-Free Interfaces. *Z. Anorg. Allg. Chem.* **2011**, *637*, 1676−1679.
(39) Zhang, P. P.; Peng, J.; Pang, H. J.; Sha, J. Q.; Zhu, M.; Wang, D. D.; Liu, M. G.; Su, Z. M. An interpenetrating architecture based on the Wells−Dawson polyoxometalate and AgI··· AgI interactions. *Cryst. Growth Des.* **2011**, *11*, 2736−2742.
(40) Fong, R.; Sacken, U.; Dahn, J. R. Studies of Lithium Intercalation into Carbons Using Nonaqueous Electrochemical Cells. *J. Electrochem. Soc.* **1990**, *137*, 2009−2013.
(41) Wei, T.; Zhang, M.; Wu, P.; Tang, Y.-J.; Li, S.-L.; Shen, F.-C.; Wang, X.-L.; Zhou, X.-P.; Lan, Y.-Q. POM-based metal-organic framework/reduced graphene oxide nanocomposites with hybrid behavior of battery-supercapacitor for superior lithium storage. *Nano Energy* **2017**, *34*, 205−214.

DOI: 10.1021/acs.inorgchem.7b00995
Inorg. Chem. 2017, 56, 8311−8318